Breast Cancer Research

RESEARCH **Open Access**

Investigating the mechanism of inositol against paclitaxel chemoresistance on triple-negative breast cancer by using 7T multiparametric MRI and mitochondrial changes

Wentao Xuan[1†], Wangmin Li[1†], Lixin Ke[1], Yuanyu Shen[1], Xiaolei Zhang[1], Yue Chen[1], Zhiliang Ye[1], Caiyu Zhuang[1], Shiyan Xie[1], Renhua Wu[1] and Yan Lin[1*]

Abstract

Background The emerging triple-negative breast cancer (TNBC) treatments target mitochondrial fission to combat paclitaxel (PTX) resistance. Inositol's inhibition of this process makes it a potential therapy. Multiparametric MRI provides an early and effective assessment of these innovations.

Objective To monitor the efficacy of Inositol on PTX-resistant TNBC mice using 7T multiparametric MRI, and to further explore the mechanism of inositol inhibiting PTX chemoresistance in combination with the morphological changes of isolated mitochondria.

Materials and methods BALB/c mice aged 6–8 weeks were subcutaneously inoculated with PTX-resistant 4T1 cells and divided into three groups: PTX-treated mice ($n=24$), "PTX + Inositol"-treated mice ($n=24$) and untreated mice ($n=24$). Six mice in each group underwent diffused weighted imaging (DWI) and diffusion kurtosis imaging (DKI) every 7 days after administration. To observe the dynamic changes of inositol within the tumor tissue post-treatment, chemical exchange saturation transfer (CEST) imaging was performed. Six mice in each group were sacrificed on day 0, 7, and 14 respectively for histopathological examination. After a 3-week scanning cycle, the remaining mice in each group were euthanized for histopathological analysis. The therapeutic response of inositol was assessed via Hematoxylin & Eosin (H&E) staining and Ki-67 immunohistochemistry. The effects of inositol on mitochondrial structure and PTX resistance were studied by Western Blot and electron microscopy. One-way analysis of variance, independent samples t-test, paired samples t-test, Kruskal-Wallis, and Spearman rank correlation were used.

Results The CEST signal of inositol in tumor tissue was significantly higher after 1 h of inositol administration than before (2.75 ± 0.71% vs. 1.80 ± 0.33%, $p<0.05$). On day 21 after treatment, the tumor volume in the PTX + Ins group

---

[†] Wentao Xuan and Wangmin Li share equal authorship of this article.

*Correspondence:
Yan Lin
ylin1@stu.edu.cn

Full list of author information is available at the end of the article

was smaller than that in the PTX group (191.52 ± 27.98 mm^3 vs. 388.98 ± 32.62 mm^3, $p < 0.001$). The MD, MK, and ADC values were correlated significantly with tumor cell density (MD, r = -0.872; MK, $r = 0.723$; ADC, r = -0.858) and Ki-67 level (MD, r = -0.975; MK, $r = 0.680$; ADC, r = -0.860). The p-AMPK levels of PTX + Ins group were lower than that of PTX group (0.50 ± 0.06 vs. 0.60 ± 0.05, $p = 0.04$), and the mitochondrial length was longer than that of PTX group (0.86 ± 0.10 vs. 0.44 ± 0.09, $p < 0.001$), with a significant correlation to Ki-67 levels (r = -0.853, $p < 0.001$).

Conclusion Inositol may counteract PTX resistance in TNBC by disrupting mitochondrial fission, and DWI combined with DKI effectively tracked this effect.

Keywords Triple-negative breast cancer, Paclitaxel resistance, Mitochondrial dynamics, Inositol, Multiparametric MRI

Introduction

Triple-negative breast cancer (TNBC) is a characteristic subtype of breast cancer featuring the negative expression of estrogen receptor, progesterone receptor, as well as human epidermal growth factor receptor-2 [1]. Chemotherapy remains the primary treatment for TNBC due to the lack of specific therapeutic targets [2, 3]. Meanwhile, recent advances in immunotherapy (e.g., PD-1/PD-L1 inhibitors) have expanded therapeutic options for TNBC, particularly for PD-L1-positive patients [4]. Although chemotherapy combined with immunotherapy may enhance treatment efficacy in selected populations [5], the treatment of advanced TNBC still relies predominantly on chemotherapy. However, the progression of the disease leads to resistance to chemotherapy, especially to paclitaxel (PTX) and anthracycline-based treatments, which significantly increases the risk of treatment failure, with failure rates potentially reaching up to 90% during the metastatic stage [6]. Hence, there is an urgent need to explore new therapeutic targets to enhance treatment efficacy and successfully fight against chemoresistance to TNBC.

Recent studies have indicated that enhanced mitochondrial fission is common in drug-resistant cells of various cancers, such as melanoma and breast cancer [7]. This increase was linked to metabolic changes, faster cell cycle progression, and greater potential for invasion and metastasis, suggesting that mitochondrial dysfunction is a potentially universal mechanism for drug resistance [8]. Farrand et al. have demonstrated that resveratrol may mitigate cisplatin resistance in ovarian cancer patients by modulating mitochondrial fission dynamics [9]. Therefore, the investigation of mitochondrial function has emerged as a significant area of interest to overcome chemotherapy resistance [10].

Paclitaxel (PTX) is a commonly used cytotoxic agent for the treatment of early-stage breast cancer. Kordias et al. provided compelling evidence that inositol metabolism is significantly reduced in paclitaxel-resistant TNBC cells, highlighting its potential as a pivotal marker of resistance [11]. Inositol plays a crucial in signal transduction and energy metabolism, and its derivatives also display anticancer properties that inhibit tumor proliferation [12]. Recent studies have shown that inositol directly restricts the activation of AMP-activated protein kinase (AMPK) to inhibit mitochondrial fission [13]. However, its role in overcoming PTX resistance in cancer cells, specifically inhibiting mitochondrial fission, is still being studied. Furthermore, the application of advanced imaging modalities to monitor the therapeutic response of tumors is pivotal in evaluating the effectiveness of specifically targeting inositol-mediated mitochondrial fission in cancer therapy. Multi-parameter MRI, including diffusion-weighted imaging (DWI), diffusion kurtosis imaging (DKI), and chemical exchange saturation transfer (CEST), significantly improves the precision of treatment evaluation by capturing treatment-induced microstructural alterations (such as chemotherapy-driven necrosis, reduced cellularity due to apoptosis, stromal fibrosis) and metabolic alterations within tumor tissue [14–20]. DWI provides non-invasive insights into cellular microstructures via apparent diffusion coefficient (ADC), offering critical data beyond conventional imaging [21–23]. DKI is a non-Gaussian model that capture tissue heterogeneity through indicators such as mean kurtosis (MK) and mean diffusivity (MD), effectively characterizing tumor microstructural complexity and serving as a promising biomarker for therapeutic efficacy evaluation [24]. Additionally, CEST MRI enhances the detection of low-concentration molecules by applying selective radiofrequency saturation pulses on exchangeable protons, allowing for the real-time monitoring of target metabolites within tumors [25, 26]. Whereas conventional DWI/DKI can be implemented on clinical 3T scanners, CEST imaging requires high-field (7T) MRI to leverage inherent SNR/CNR advantages and the prolonged T1 relaxation times, thereby amplifying the CEST signals, which is critical for detecting therapeutic responses [27].

Inositol is a key differentiating metabolite between PTX-resistant and non-resistant TNBC cells and can directly inhibit mitochondrial fission [11, 13]. However, its role in inhibiting PTX chemoresistance via mitochondrial fission suppression remains unclear. Furthermore, the traditional evaluation of tumor efficacy based on size changes has limitations in early response evaluation. Hence, the purpose of this study was to dynamically monitor the efficacy of inositol on PTX-resistant TNBC mice using Multi-parameter MRI and further explore the mechanism of inositol inhibiting PTX chemoresistance in combination with the morphological changes of isolated mitochondria.

Materials and methods

The overall experimental design

Figure 1 depicted the overall experimental design. To investigate the effect of inositol on paclitaxel-resistant TNBC, we first established a paclitaxel-resistant cell line as a research model. Subsequently, tumor xenografts were grown in female BALB/c mice and multiparametric MRI imaging was performed to gain insight into tumor response to treatment. Following imaging, the tumor was resected and the tumor proliferation, p-AMPK protein expression, and mitochondrial morphology were analyzed by immunohistochemistry, Western blot analysis, and transmission electron microscopy.

Cell culture and generation of paclitaxel-resistant cell line

The 4T1 breast cancer cells (China Center for Type Culture Collection, Wuhan, China) were cultured to construct an animal model of paclitaxel-resistant breast cancer for subsequent study. The cells were cultured in Dulbecco's modified Eagle's medium (DMEM) supplemented with 10% fetal bovine serum (FBS) and 1% penicillin and streptomycin at 37 °C and 5% CO2. A PTX-resistant 4T1 cell line was then generated from parental lineages through the high-dose paclitaxel pulse method. After logarithmic growth, the cells were exposed to paclitaxel at IC50 concentrations for 48 h. Following exposure, the cells were washed twice with PBS to remove residual drugs and dead cells, then the medium was replaced with fresh medium every 1–2 days. Following recovery, the cells underwent repeated paclitaxel pulsing for more than 30 generations using the identical protocol.

Animal preparation

All animal experiments were performed in accordance with the ARRIVE guidelines and the National Institutes of Health guide for the care and use of Laboratory animals (NIH Publications No. 8023, revised 1978) and approved by the Animal Ethics Committee of Shantou University Medical College (2021 – 500), China. Six-week-old female BALB/c mice ($n = 72$; Charles River Huasheng Biotechnology Co., Ltd., Guangzhou, China) were subcutaneously implanted with 1×10^6 PTX-resistant 4T1 breast cancer cells in the right hind flank. Two weeks after cell implantation, 72 tumor-bearing mice were randomized into three groups: PTX-treated mice (PTX, $n = 24$), "PTX + Inositol"-treated mice (PTX + Ins, $n = 24$), and untreated mice (control, $n = 24$). Mice in the PTX group were intraperitoneally injected with PTX (10 mg/kg dissolved in DMSO) every other day for a total of 6 times. The PTX + Ins group was treated with the same PTX regimen followed by daily administration of inositol at a dose of 80 mg/kg for 21 days. The control group did not receive any treatment. In order to evaluate the therapeutic effect of inositol at different time points in the course of treatment, six mice in each group were sacrificed on day 0, 7, and 14 respectively for histopathological examination, and then the remaining mice in each group were euthanized after a 3-week scanning cycle for histopathological analysis.

In vivo toxicity assessment

Ten BALB/c mice with an average body weight of 20 g were used for in vivo toxicity evaluation, of which 5 were in the control group and only normal saline was given via

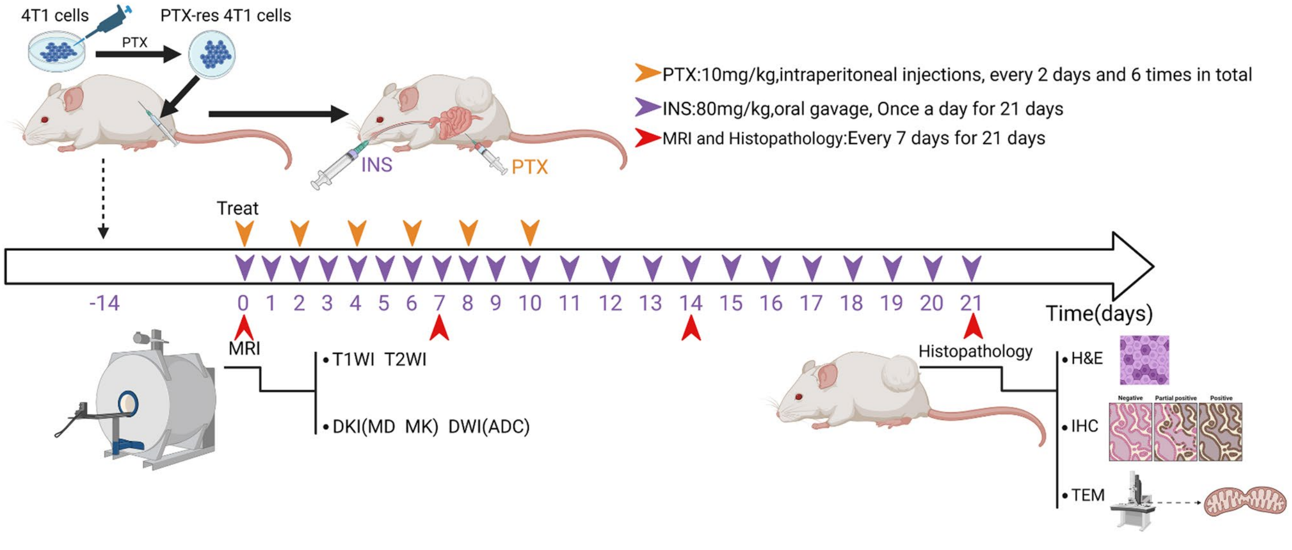

Fig. 1 Flowchart of the study

gavage, and the other 5 were in the Ins group and the dosage of intragastric inositol was 80 mg/kg once daily for 21 days. Tissue and blood samples were collected from both groups of mice. Hematoxylin and eosin (H&E) staining of the heart, liver, spleen, and kidney tissues of the mice was performed. Four important hepatic indicators (alanine aminotransferase [ALT], aspartate aminotransferase [AST], alkaline phosphatase [ALP], and total protein [TP]), and three indicators of renal function (creatinine [CRE], blood urea nitrogen [BUN], and urea [UA]) were determined.

7T multiparametric MRI

All imaging procedures in this study were performed on an Agilent 7.0 T MR system (Agilent Technologies, Santa Clara, CA, USA) with a standard 9563 body coil for signal transmission and reception.

In vitro chemical exchange saturation transfer (CEST) imaging of inositol

Different concentrations of inositol (5 mM, 15 mM, 25 mM, and 35 mM) were prepared at the same pH 7.0 for CEST scanning. To evaluate whether the CEST effect of inositol is pH-dependent, five solutions with different pH values (6.2, 6.5, 6.8, 7.1, and 7.4) were titrated at the same concentration (25 mM). The optimum conditions were determined by different saturation powers (1 to 3.5 μT) and different saturation times (2 to 6 s). For the in vitro CEST imaging, a continuous wave echo planar imaging (CW-EPI) sequence was used with the following parameters: repetition time /echo time (TR/TE), 6000/29 msec; section thickness, 2 mm; field of view (FOV), 30 × 30 mm^2; k-space central line number (kzero), 32; matrix size, 64 × 64; acquisition time, 13 min.

In vivo MR imaging

Mice were imaged with a 7.0T MR imaging unit using an abdominal coil while being anesthetized with 2.5-3% isoflurane gas, and their respiratory rate was monitored during examinations. The MRI protocols incorporated a three-plane localizer, axial T2-weighted imaging (T2WI), DKI, DWI, and CEST imaging. The fast spin echo (FSE) T2WI scan parameters were as follows: TR/TE, 2000/24.2 msec; section thickness, 2 mm; FOV, 30 × 30 mm^2; matrix size, 128 × 128, acquisition time, 1.5 min. The DKI acquisition parameters were as follows: TR/TE, 2000/86 msec; matrix, 128 × 128; section thickness, 2 mm; FOV, 36 × 30 mm^2; section thickness, 2 mm; b values = 0, 1000, and 2000 s/mm^2; acquisition time, 4 min. Parameters for DW imaging were as follows: TR/TE, 2000/24 msec; matrix, 96 × 96; section thickness, 2 mm; FOV, 36 × 30 mm^2; b values = 0 and 1000 s/mm^2; acquisition time, 2 minutes. Single-shot echo planar imaging sequence with continuous-wave saturation pulse (B1 = 2.5μT, pulse width = 4s) was used to obtain the Ins CEST images with the following parameters for the selected plane: TR/TE, 6000/26 msec; flip angle, 30°; section thickness, 2 mm; FOV, 36 × 30 mm^2; kzero, 32; the number of shots, 1; matrix size = 64 × 64; acquisition time, 13 min. Post-processing of the DWI, DKI, and CEST images were performed using MATLAB (MathWorks, Natick, Massachusetts) and ImageJ (National Institutes of Health, Bethesda, Maryland).

Image post-processing and quantitative parameter analysis

Post-processing of the DWI, DKI, and CEST images were performed using MATLAB (MathWorks, Natick, Massachusetts; commercial software) for parametric mapping and ImageJ (National Institutes of Health, Bethesda, Maryland; open-source) for regions of interest (ROI) analysis. Tumor volume quantification was derived from T2-weighted images through elliptical approximation ($V = a \times b^2/2$, a = long-axis diameter and b = orthogonal short-axis diameter) [28]. All DKI and DWI data were postprocessed using open-source scripts in MATLAB, which automatically generated parametric maps of MK, MD, and ADC. ADC maps were derived from DWI (b = 0, 1000 s/mm^2) using the mono-exponential model with the equation [29]: $\ln(S_b) = \ln(S_0) - \text{bADC}$, where S_0 is the signal intensity without diffusion-weighting, S_b is the signal intensity with diffusion-weighting, b is the applied diffusion sensitization (s/mm2). The MD and MK values were calculated with the following equation: $S_b = S_0 \times \exp(-b \times D + 1/6 \times b^2 \times D^2 \times K)$, where S_b is the diffusion signal intensity with particular b values, S_0 is the baseline signal without diffusion weighting, D is the diffusion coefficient with correction of non-Gaussian distribution bias, and K is a dimensionless metric. Parametric maps were co-registered to anatomical T2WI using ROI-based alignment in ImageJ, where manually defined ROIs were replicated from T2 templates to parameter maps for spatial consistency. Regions of ROIs were manually delineated on co-registered parameter maps using ImageJ software at the lesion's maximum cross-sectional plane with necrotic regions exclusion, ultimately deriving mean parameter values through ROI histogram analysis. All CEST image processing and data analysis were performed using custom-written scripts in MATLAB. Regions of interest were drawn manually based on the T2-weighted images covering the entire tumor. The CEST contrast was quantified by determining MTRasym, as defined by the following expression [30, 31]:

$$MTR_{asym} = \frac{S_{sat}(-\Delta\omega) - S_{sat}(+\Delta\omega)}{S_0},$$

where $S_{sat}(+\Delta\omega)$ and $S_{sat}(-\Delta\omega)$ are the signal intensities obtained by saturating at the frequency of $\Delta\omega$ downfield and upfield from the water proton resonance frequency, respectively. S_0 is the water signal intensity in the absence of the saturation pulse.

Ex vivo tissue analysis

The resected tumor was fixed with 4% paraformaldehyde at 4 °C for 24 h. Serial 5-mm-thick paraffin slices were made for H&E staining to evaluate the degree of necrosis and the number of viable tumor cells. In immunohistochemical analysis, the sections were stained with Ki-67 to determine the proliferative activity within the tumor specimens. The tumor cell density was determined by calculating the ratio of the tumor cell area to the total area on the maximum cross-section. The Ki-67 index was quantified by counting the number of Ki-67-positive cells and their percentage of the total number of cells within the tumor sections. The levels of phosphorylated AMP-activated protein kinase (p-AMPK) in tumor tissues were quantified by Western blot analysis. The mitochondrial morphology of tumor tissues was assessed using transmission electron microscopy (TEM) (HT7700, Hitachi, Ltd., Tokyo, Japan).

For quantitative histopathological evaluation, three non-consecutive and non-overlapping fields were systematically selected from representative tumor regions using randomized sampling methodology. Tumor cell density was calculated as the percentage of neoplastic cell area to total cross-sectional area in H&E-stained sections through automated threshold segmentation with ImageJ software. In immunohistochemical analysis, Ki-67 proliferation indices were determined by quantifying the proportion of positively stained nuclei relative to total cellularity across randomly chosen fields. Western blot quantification of p-AMPK expression involved grayscale normalization against β-actin controls using background-subtracted densitometry. Ultrastructural assessment of mitochondrial morphology incorporated measurements of longitudinal axis length for discrete organelles per sample via calibrated scale analysis in ImageJ.

Statistical analysis

All statistical analyses were performed by using the SPSS 25.0 software package (SPSS, Inc., Chicago, IL). The normality of data was tested with the Kolmogorov-Smirnov test. The statistical significance of the differences of CEST signals before and after treatment was determined by paired t-test. To compare MR imaging metrics (MD, MK, ADC), histological parameters (tumor cell density, Ki-67 index), and tumor growths, one-way repeated measure analysis of variance (ANOVA) was performed, and Bonferroni post-hoc correction was applied for all pair comparisons. The Kruskal-Wallis test was utilized for analyzing non-normally distributed data involving multiple samples. Correlation between histological parameters (tumor cell density, Ki-67 index) and MR imaging metrics (MD, MK, ADC) were assessed with the Spearman correlation coefficient. $p < 0.05$ was considered to indicate a statistically significant difference. All data were reported as means ± standard deviations unless otherwise indicated.

Results

Establishment of paclitaxel-resistant TNBC mouse model

A PTX-resistant TNBC mouse model was established using 4T1 cell lines with repeated high-dose PTX exposure. As the dose of paclitaxel increased, the viability of the derived cell lines declined more slowly, indicating increased resistance (Figure S1A). Its resistance was more than 10 times higher than that of the parental cells, with IC50 values of 26 μM and 2 μM, respectively (Figure S1B). Drug-resistant cells were implanted subcutaneously in the right flank of mice to establish a model, which laid a foundation for studying mechanisms to overcome PTX resistance in TNBC.

Inositol has excellent biocompatibility via toxicity studies

After administering 80 mg/kg of inositol intragastrically for 21 days, no behavioral abnormalities were observed in all mice. Liver (ALT, AST, ALP, TP) and kidney function (CRE, BUN, UA) indicators were all within the normal range (Figure S2). H&E staining of heart, liver, spleen, and kidney showed no adverse effects (Figure S3).

Characterization of inositol in CEST imaging and biodistribution

The hydroxyl group on inositol generates CEST effect at a selective saturation of 0.6 ppm (Figure S4). To monitor the dynamic changes and biodistribution of inositol in tumors, in vitro and in vivo CEST imaging studies were conducted. In vitro CEST imaging showed a concentration-dependent increase in CEST signal, from 11.76% (5 mM) to 27.18% (35 mM) (Fig. 2A, B). CEST signal also demonstrated pH sensitivity, increasing from 12.90% at pH 7.4 to 29.61% at pH 6.2, indicating suitability for the study of the acidic tumor microenvironments. Furthermore, the CEST effect of inositol was increased with the increase of saturation power and time in a certain range and reached its peak value at a saturation power of 2.5 μT and a saturation pulse of 4 s. In vivo CEST imaging showed an increased CEST signal of inositol in mouse tumors compared to baseline (Fig. 2C). Quantitative analysis revealed that the CEST signal of inositol peaked at around 1 h post-administration (2.75% ± 0.71%), significantly higher than the baseline value (1.80% ± 0.33%, $p = 0.04$) (Fig. 2D).

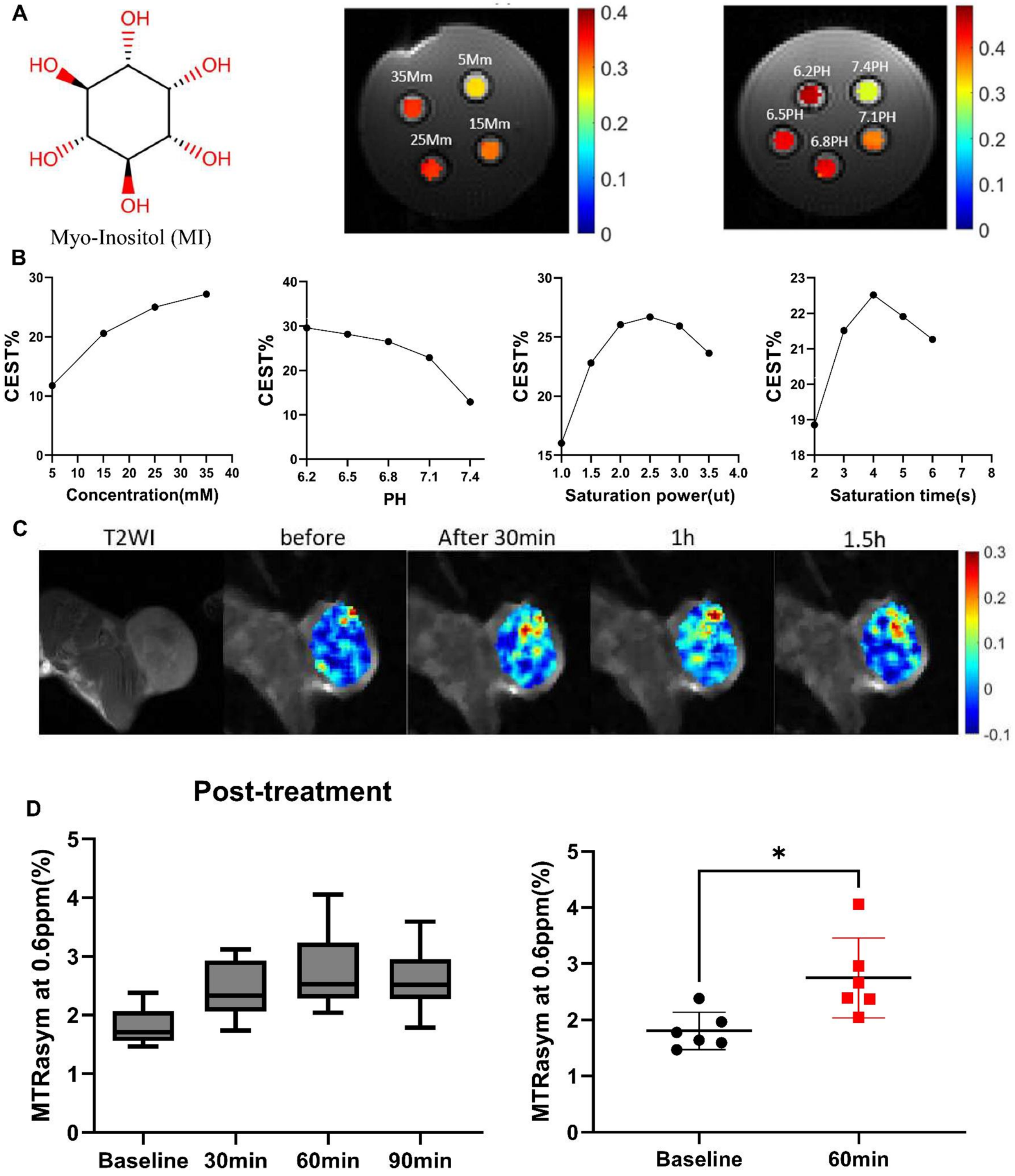

Fig. 2 Inositol structure, CEST imaging features, and biodistribution. **A**, Chemical structure of inositol, and CEST imaging of inositol at different concentration and pH, showing that the CEST effects of inositol were both concentration and pH-dependent; **B**, The impact of varying concentrations, pH values, and scanning parameters on the CEST effect of inositol. **C**, Representative T2-weighted images (T2WI) and CEST images before inositol treatment, and CEST images at 30, 60, and 90 min after treatment. D, Representative dynamic time course of CEST effect of inositol in mouse tumors after treatment. Statistical significance: *$p < 0.05$. Central dark band = mean, whiskers = standard deviation

Comparison of tumor volume and imaging parameters (MD, MK, and ADC) between the PTX group, PTX + Ins group, and control group

In order to assess early changes in efficacy following tumor treatment, multiparametric MRI scans were performed on tumor-bearing mice at various time points. Tumor volume and MRI signals (T2WI, DWI, and DKI) in untreated control group ($n = 6$), PTX-treated group ($n = 6$), and PTX + Ins treated group ($n = 6$) were monitored, respectively (Fig. 3A). At baseline, all groups had similar tumor morphology and signaling. On day 21 post-treatment, the tumors in the PTX + Ins group were significantly smaller than those in the control group and PTX group. The tumor volume, MD, MK, and ADC of different groups were quantified at different time points to compare the dynamic changes (Fig. 3B). PTX treatment alone did not significantly inhibit tumor growth, while the tumor growth rate in the PTX + Ins group was slower. The average tumor volume in the control and PTX groups on day 21 was 388.98 ± 32.26 mm^3 and 400.61 ± 76.00 mm^3, respectively, while that of the PTX + Ins group was only 191.52 ± 27.99 mm^3, which showed a significant difference compared with the control group and the PTX group ($p < 0.001$) The results of tumor volume measurement were shown in Supplementary Table S1.

As shown in Fig. 3B, the MD and ADC values in the PTX group exhibited an upward trend, peaking at day 7 (1.02 ± 0.07 and 1.09 ± 0.14, respectively), which were significantly higher than those in the control group (0.69 ± 0.04, $P < 0.001$ and 0.67 ± 0.03, $p < 0.001$, respectively). The MD and ADC values of PTX group at day 14 (0.80 ± 0.12 and 0.81 ± 0.15, respectively) were significantly lower than those at day 7 ($p = 0.004$ and $p = 0.007$, respectively). However, there was no significant difference at day 14 when compared with the control group. The MD and ADC values in the PTX + Ins group showed similar dynamic changes as those in the PTX group, but the duration of increase was longer, reaching the highest values on day 14 (1.31 ± 0.39 and 1.33 ± 0.27, respectively), and the difference was statistically significant compared with those in the PTX group ($p < 0.01$ and $p < 0.001$, respectively). Although MD and ADC values in the PTX + Ins group decreased over time after day 14, they remained significantly higher than those in the control and PTX groups until the end of the scans. The MK value of PTX + Ins group was continuously lower than that of control group. However, there was no significant difference in MK values in the PTX + Ins group at any observation time point compared to the PTX group. Details of the MD, MK, and ADC measurements were summarized in Supplementary Table S2.

Histologic analysis of tumor response after treatment at various time point

To elucidate the therapeutic effect of inositol on TNBC, histological analysis was conducted at different time

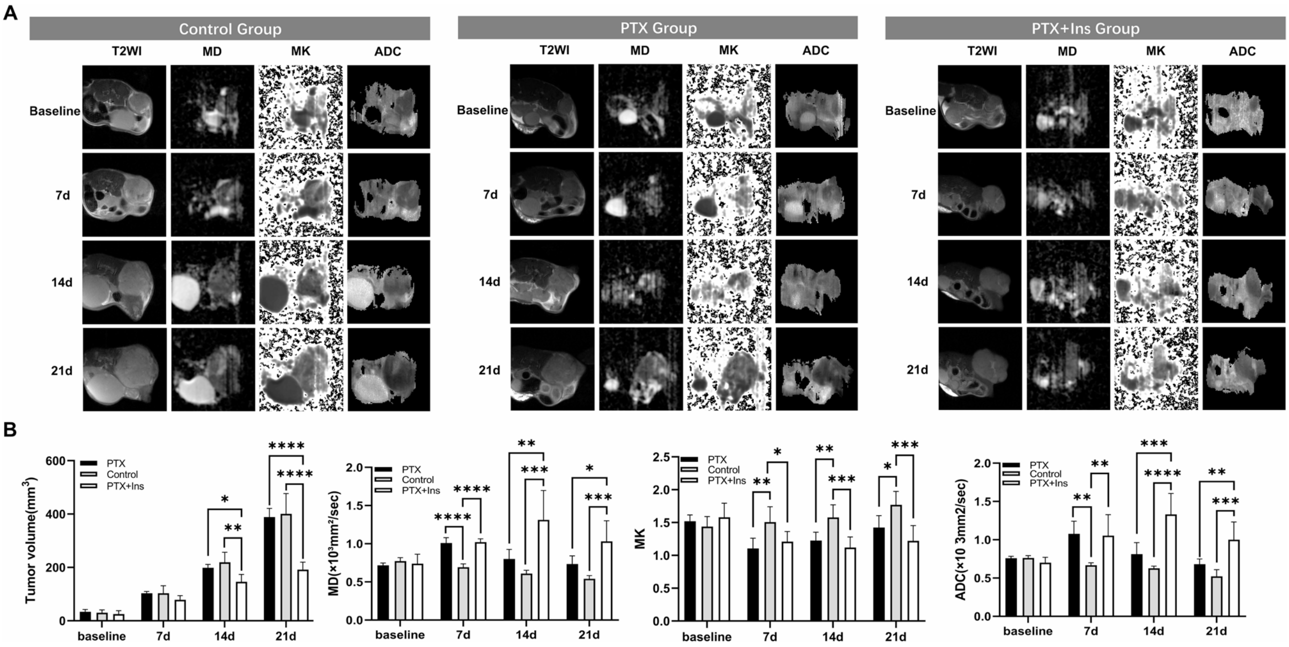

Fig. 3 The changes of tumor volume, Mean Diffusivity (MD), Mean Kurtosis (MK) and Apparent Diffusion Coefficient (ADC) in MRI scans of tumor-bearing mice at various treatment time points. **A**, Representative T2-weighted imaging (T2WI), MD, MK and ADC mapping in untreated control group, PTX-treated group and PTX + Ins treated group, respectively. **B**, The variability of tumor volumes, MD, MK, and ADC values among different groups at different time points. One-way ANOVA with Bonferroni post-hoc correction was performed for statistical analysis. Statistical significance: *$p < 0.05$, **$p < 0.01$, ***$p < 0.001$, ****$p < 0.0001$. The error bars are standard deviation

points in each group. As shown in Fig. 4A, H&E staining of control group revealed round or oval tumor cells with protruding nuclei and numerous mitotic figures, while the PTX group exhibited central necrosis on day 7 and new solid tumor components within necrotic area on day 14. Subsequently, the tumor cells in the PTX group grew increasingly dense over time. In the PTX + Ins group, the central necrosis peak occurred on day 14, and new solid tumor components were formed on day 21 (Fig. 4A). Ki-67 staining indicated positive expression of dark

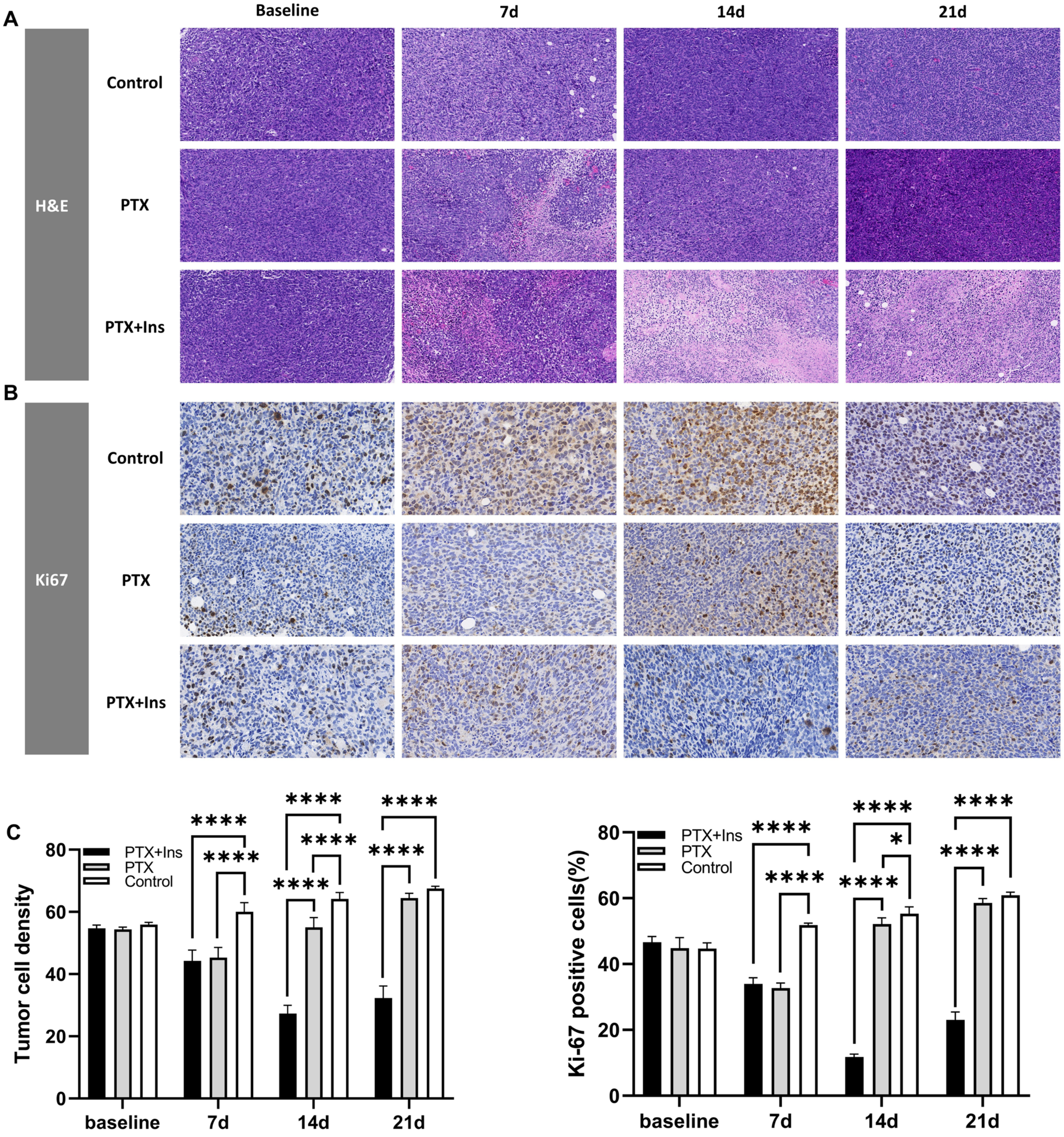

Fig. 4 Histologic examination of tumor response at different time point after treatment in each group. **A**, High magnification scan of hematoxylin-eosin–staining (amplification ×20). **B**, Scan of Ki-67 immunohistochemistry staining with high magnification (amplification ×40). The brown-stained particles represent the Ki-67-positive expression region. **C**, Quantitative analysis of tumor cell density and Ki-67 expression in different groups of mice. One-way ANOVA with Bonferroni post-hoc correction was performed for statistical analysis. Statistical significance: $^{*}p < 0.05$, $^{**}p < 0.01$, $^{***}p < 0.001$, $^{****}p < 0.0001$. The error bars are standard deviation

brown nuclei. In the PTX group, the proportion of Ki-67 positive cells reached its lowest point on day 7 and then began to increase. In the PTX + Ins group, the proportion of Ki-67 positive cells reached its lowest point on day 14 and then started to rise (Fig. 4B). Quantitative analysis revealed that tumor cell density and Ki-67 staining decreased gradually in the PTX + Ins group, reaching the lowest point on day 14 (Fig. 4C). Tumor cell density and Ki-67 staining were significantly lower in the PTX + Ins group than in the other two groups on days 14 and 21. These observations suggested that the PTX + Ins group demonstrated superior efficacy than the control group and PTX group.

Correlation of MR imaging and histologic biomarkers

To evaluate the feasibility of MD, MK, and ADC as predictors of tumor therapeutic response, the correlation between the histologic features and MRI parameters were assessed. The MRI parameters on day 21 showed a statistically significant correlation with the corresponding histologic features. Tumor cell density was significantly correlated with ADC (r = -0.858, $p < 0.001$), MD (r = -0.872, $p < 0.001$), and MK ($r = 0.723$, $p < 0.001$), respectively (Fig. 5A). The Ki-67 index showed a significant correlation with ADC (r = -0.860, $p < 0.001$), MD (r = -0.975, $p < 0.001$), and MK ($r = 0.680$, $p = 0.002$), respectively (Fig. 5B).

AMPK suppression by treatment group

Western blot analysis of tumor slices 21 days post-therapy showed that phosphorylated AMPK (p-AMPK) levels in the PTX + Ins group (0.50 ± 0.06) were lower compared to the PTX group (0.60 ± 0.05, $p = 0.04$) (Fig. 6A, B). Transmission electron microscopy revealed fewer atrophied and fragmented mitochondria in the PTX + Ins group compared to the PTX group (Fig. 6C). The mitochondrial length of PTX + Ins group (0.86 ± 0.10) was significantly longer than that of PTX group (0.44 ± 0.09; $p < 0.001$). Additionally, mitochondrial length was significantly negatively correlated with Ki-67 index (r = -0.853, $p < 0.001$) (Fig. 6D), indicating that inositol might counteract drug resistance by inhibiting mitochondria function.

Discussion

The therapeutic potential of inositol in overcoming drug resistance in TNBC remains unexplored. Previous studies have revealed that dysregulated inositol metabolism contributed to cancer progression, especially in paclitaxel-resistant TNBC cells, where inositol levels were reduced and mitochondrial fission was enhanced compared to the TNBC non-resistant cells [11, 13]. In this study, we successfully demonstrated the potential of inositol in overcoming paclitaxel resistance in TNBC therapy through 7T multiparametric MRI combined with the observation of mitochondrial morphological changes, and also provided an early, non-invasive and effective evaluation method for TNBC effective treatment.

Unlike previous studies that tracked inositol using radiolabels [32], our study utilized CEST imaging, a non-invasive, non-radioactive method that allows real-time tracking of treatment dynamics, to monitor inositol distribution in tumors [33]. In inositol treated mice, CEST signals in tumors increased over time, peaking about an hour after administration, indicating rapid penetration

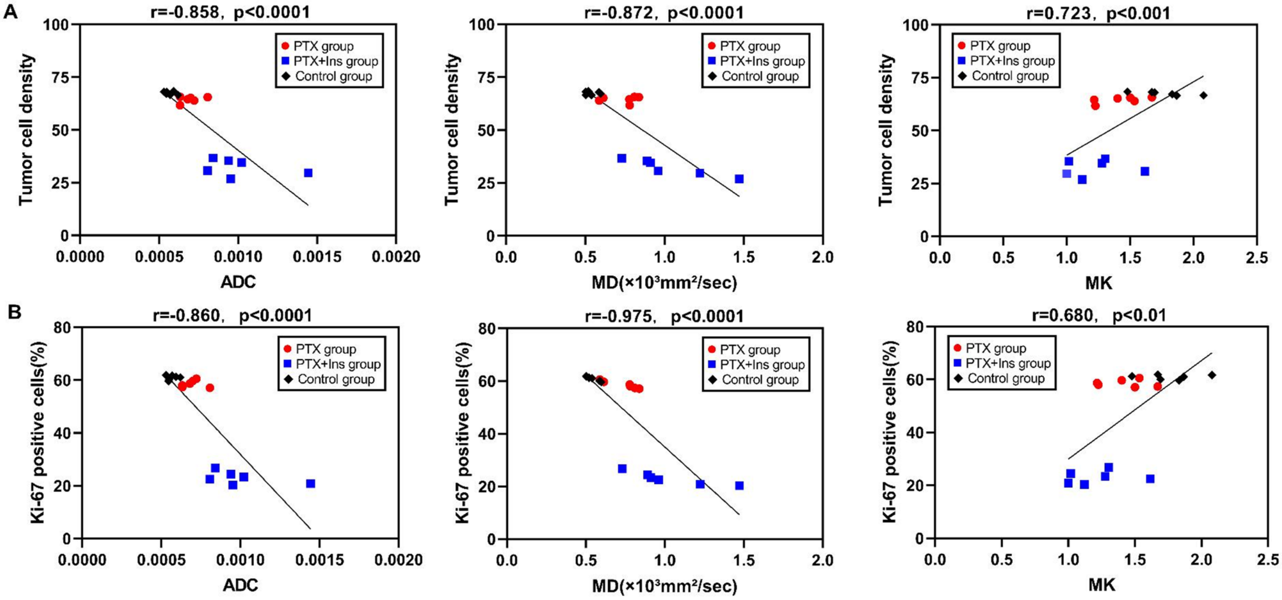

Fig. 5 Spearman correlation between the MRI parameters and histologic features in each group on day 21. **A**, Correlation between tumor cell density and ADC, MD, and MK. **B**, Correlation between Ki-67 index and ADC, MD, and MK

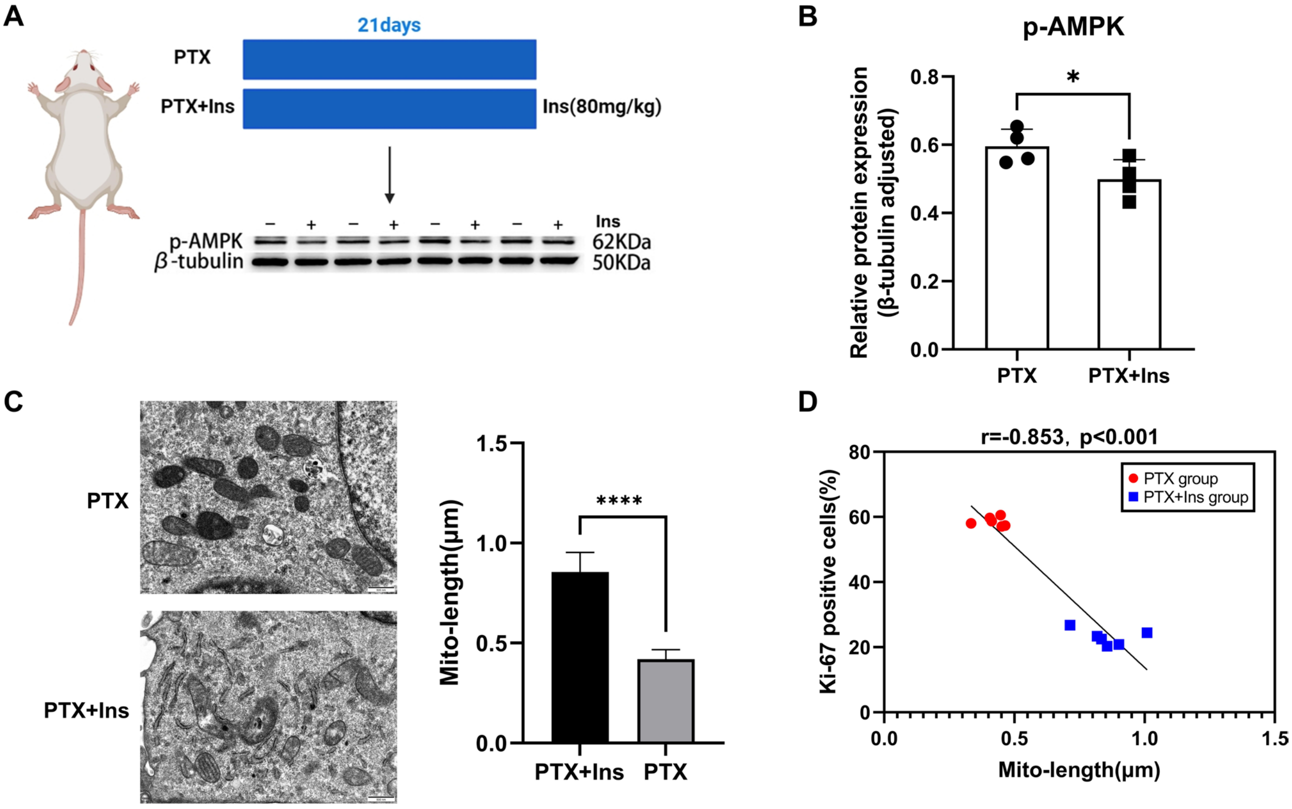

Fig. 6 Comparative Analysis of AMPK Activity, Mitochondrial Fission, and Tumor Cell Proliferation between PTX and PTX + Ins Groups at 21 Days Post-Treatment. **A**, The protein extract from tumor tissues was subjected to Immunoblotting. **B**, Histogram of relative protein expression between PTX + Ins group ($n = 4$) and PTX group ($n = 4$). **C**, Transmission electron microscopy (TEM) imaging (scale 500 nm) of tumor tissues in control and treatment group mice. **D**, The correlation between the change in mitochondrial length on day 21 and the density of cells expressing Ki-67. Statistical significance: $^{*}p < 0.05$, $^{****}p < 0.0001$. The error bars are standard deviation

and gradual accumulation of inositol in tumor tissue. These results aligned with previous findings on rapid absorption and short systemic circulation of small molecules such as inositol, suggesting that small molecules are rapidly distributed from the gastrointestinal tract to distant tumor sites after oral administration [34, 35]. Our study demonstrated that CEST imagings has great potential for clinical applications to monitor drug distribution within tumors.

Traditional imaging methods that assess tumor morphology may not be able to show treatment effects in a timely manner, as functional changes in the tumor often precede visible morphological changes [36, 37]. We evaluated treatment response to PTX-resistant TNBC by tracking tumor volume and using advanced DWI/DKI metrics. In this study, PTX + Ins, PTX, and control groups had similar tumor volumes on day 7, but there were significant differences in MD, MK, and ADC values between them. This highlights the advantages of multiparametric functional MRI, which is capable of detecting early physiological and molecular changes, thus enabling a more rapid and precise assessment of treatment response before any visible tumor alterations occur [38, 39].

Changes in tumor volume showed that PTX monotherapy had a negligible effect on tumor growth, similar to that of the control group. However, PTX + Ins therapy significantly slowed tumor progression, especially on days 14 and 21, indicating improved efficacy in overcoming PTX resistance. Additionally, the PTX + Ins group exhibited a notable peak in MD and ADC values on day 14, which may be due to the increased apoptosis and cell structural changes induced by combination therapy, resulting in increasd diffusivity of water molecular [18, 39]. In contrast, MD and ADC values in the PTX group exhibited an initial peak on day 7 followed by a rapid decline, underscoring the limited and transient efficacy of paclitaxel monotherapy. The MK parameter represents the deviation of the diffusion property from Gaussian behavior, reflecting in detail the complexity of the microstructure [29, 40, 41]. The treatment group showed reduced MK values compared to the control group, indicating a reduction in the complexity of the tumor microstructure during treatment. However, the differences in MK values between combination therapy and PTX alone is small, which implied a limited sensitivity of MK in assessing the efficacy of treatment. Taken together, the data suggested that PTX + Ins combination therapy may provide better tumor control compared to PTX monotherapy, and ADC and MD values potentially serve as early predictors of therapeutic effect.

Our present study confirmed through histological analysis that inositol combined with paclitaxel (PTX + Ins) could overcome paclitaxel resistance in TNBC, and the changes of DKI and DWI parameters were consistent with pathological findings. Correlation analysis on day 21 revealed that tumor cell density and Ki-67 levels were negatively correlated with ADC and MD values, and positively correlated with MK values. This was due to the enhanced diffusion of water molecules during apoptosis, ADC and MD values increased with the decrease of cell density and proliferation (reflected as a decrease of Ki-67), while MK values decreased with the decrease of tissue complexity during apoptosis, and were therefore positively correlated with the declining cell density and Ki-67 levels. It has been reported that MK has a higher value in predicting tumor aggressiveness than ADC [29]. However, the correlation coefficient between MK value and pathological results was lower compared to MD and ADC, which may be due to the large heterogeneity of tumor tissues, resulting in the instability of MK value. Furthermore, DKI-MD exhibits a higher sensitivity than DWI-ADC in detecting microstructural changes. This might be attributed to the higher spatial resolution of DKI (128 × 128 matrix) than DWI (96 × 96 matrix) under identical FOV, rather than an inherent advantage of the model itself. All in all, the relationships between MD, MK, and ADC parameters and tumor cell density and Ki-67 index suggested that these imaging techniques provided valuable insights into tumor activity and treatment response.

Phosphorylated AMPK acts as a crucial energy sensor activated during energy deficiency, influencing mitochondrial biogenesis and fission [42, 43]. Our Western blot results showed a decrease in p-AMPK levels in the PTX + Ins group compared to the PTX group, suggesting that inositol inhibited AMPK activation during treatment. Electron microscopy revealed that inositol reduced atrophied and fragmented mitochondria and increased mitochondrial length in the PTX + Ins group, highlighting its role in preserving mitochondrial integrity [13]. These findings demonstrated that inositol inhibits mitochondrial fission by suppressing AMPK activation during treatment. Mitochondrial morphological instability, such as excessive division or fusion, can disrupt energy metabolism and promote tumor cell proliferation [44, 45]. We observed a negative correlation between mitochondrial length and Ki-67 expression, indicating that changes in mitochondrial morphology were associated with the therapeutic effect of inositol therapy. This emphasizes the link between mitochondrial structure, function, and tumor cell proliferation. These findings suggested that inositol may enhance the tumor chemosensitivity by inhibiting mitochondrial fission.

Our study had limitations. First, the TR = 2000 ms parameter setting in MRI acquisition was shorter than clinical recommendations (≥ 3000 ms) [46], which might affect signal recovery completeness, though the 7.0 T ultra-high field system could provide partial compensation through enhanced signal characteristics. Second, the spatial resolution of DWI was lower than that of DKI (96 × 96 vs. 128 × 128 matrix under the same field of view), which may have influenced the parameter performance and histopathological correlation. Due to the prolonged CEST scanning time (~ 13 min per scan) causing significant physiological stress and limited cohort size, longitudinal analyses exploring the correlation of CEST-treatment outcome were precluded. We plan to implement optimized protocols (e.g., accelerated scanning) in future studies to address this limitation. Third, the narrow cohort of mouse models used may not fully capture the complexities of human conditions. The biological differences between mice and humans need to be validated in a wider range of biological systems. Future studies should optimize MRI parameters per clinical standards, while increasing the sample size and applying a broader array of biological models to enhance the robustness and generalizability of our results. Additionally, evaluating the reproducibility of 7T multi-parametric MRI technology across various research settings is crucial to determine its suitability for clinical applications.

To advance these findings toward clinical translation, future human studies should validate inositol's efficacy and safety via Phase I/II trials, integrating multiparametric MRI biomarkers (ADC, MD) with histopathological and survival outcomes. Key translational barriers include interspecies biological discrepancies, limited accessibility of high-field MRI, and formulation optimization for inositol-paclitaxel synergy. Notably, inositol's mitochondrial stabilization may enhance immunogenicity, offering potential to complement immune checkpoint inhibitors by modulating tumor metabolic-immune crosstalk [47, 48]. Addressing these challenges while exploring combinatorial immunotherapy strategies could redefine TNBC treatment paradigms for chemoresistant patients.

Conclusions

In summary, our research combined 7T multiparametric MRI with mitochondrial morphological changes and found that inositol enhanced the therapeutic sensitivity of TNBC cells to paclitaxel by preserving mitochondrial integrity, thereby slowing tumor cell proliferation. This discovery highlights the therapeutic potential of inositol in combating paclitaxel resistance in TNBC, laying a valuable foundation for the development of new treatment strategies.

Abbreviations

TNBC	Triple-negative breast cancer
PTX	Paclitaxel
MRI	Magnetic resonance imaging
DWI	Diffused weighted imaging
DKI	Diffusion kurtosis imaging
CEST	Chemical exchange saturation transfer
H&E	Hematoxylin & Eosin
AMPK	AMP-activated protein kinase
ADC	Apparent diffusion coefficient
MK	Mean kurtosis
MD	Mean diffusivity
DMEM	Dulbecco's modified Eagle's medium
FBS	Fetal bovine serum
T2WI	T2-weighted imaging
TR	Repetition time
TE	Echo time
FOV	Field of view
kzero	K-space central line number
p-AMPK	Phosphorylated AMP-activated protein kinase
ANOVA	Analysis of variance
ALT	Alanine aminotransferase
AST	Aspartate aminotransferase
ALP	Alkaline phosphatase
TP	Total protein
CRE	Creatinine
BUN	Blood urea nitrogen
UA	Urea

Supplementary Information

The online version contains supplementary material available at https://doi.org/10.1186/s13058-025-02051-4.

Supplementary Material 1

Supplementary Material 2

Supplementary Material 3

Acknowledgements

The authors are grateful to Second Affiliated Hospital of Shantou University Medical College, Department of Research Center of Translational Medicine for support.

Author contributions

WX, LK, and YL drafted the manuscript; WX, YL, WL, YS, and CZ designed experiments; WX and WL performed experiments, collected data, and analyzed the data. YS, ZY, CZ, and SX assisted in the execution of experiments. RW provided essential experimental equipment and facilities. XZ and YC participated in data analysis. YL initiated the study and obtained funding for the study. WX and WL verified the underlying data of this manuscript. All authors reviewed and approved the final version of the manuscript.

Funding

This study was supported by grants from the National Natural Science Foundation of China (82071973), Basic and Applied Basic Research Foundation of Guangdong Province (2023A1515010326, 2020A1515011022) and Key Research Platform and Project of Guangdong University (2022ZDZX2020).

Data availability

All data presented in this manuscript are available from the corresponding author upon request.

Declarations

Ethics approval and consent to participate

All animal experiments were approved by the Animal Ethics Committee of Shantou University Medical College (2021 – 500), China.

Consent for publication

Not applicable.

Competing interests

The authors declare no competing interests.

Author details

[1]Radiology Department, Second Affiliated Hospital of Shantou University Medical College, Shantou, Guangdong, China

Received: 14 December 2024 / Accepted: 19 May 2025

References

1. Boyle P. Triple-negative breast cancer: epidemiological considerations and recommendations. Ann Oncol. 2012;23(Suppl 6):vi7–12.
2. Vinayak S, Tolaney SM, Schwartzberg L, Mita M, McCann G, Tan AR, et al. Open-label clinical trial of niraparib combined with pembrolizumab for treatment of advanced or metastatic Triple-Negative breast Cancer. JAMA Oncol. 2019;5(8):1132–40.
3. Dabbagh N, Riazi H, Khayamzadeh M, Negahi A, Akbari M, Akbari ME. The effect of neoadjuvant vs adjuvant chemotherapy on final outcome of patients with triple negative breast Cancer. Med J Islam Repub Iran. 2022;36:61.
4. Keenan TE, Tolaney SM. Role of immunotherapy in Triple-Negative breast Cancer. J Natl Compr Canc Netw. 2020;18(4):479–89.
5. Cortes J, Rugo HS, Cescon DW, Im SA, Yusof MM, Gallardo C, et al. Pembrolizumab plus chemotherapy in advanced Triple-Negative breast Cancer. N Engl J Med. 2022;387(3):217–26.
6. Nedeljkovic M, Damjanovic A. Mechanisms of chemotherapy resistance in Triple-Negative breast cancer-How we can rise to the challenge. Cells. 2019;8(9).
7. Rodrigues T, Ferraz LS. Therapeutic potential of targeting mitochondrial dynamics in cancer. Biochem Pharmacol. 2020;182:114282.
8. Mukherjee S, Bhatti GK, Chhabra R, Reddy PH, Bhatti JS. Targeting mitochondria as a potential therapeutic strategy against chemoresistance in cancer. Biomed Pharmacother. 2023;160:114398.
9. Farrand L, Byun S, Kim JY, Im-Aram A, Lee J, Lim S, et al. Piceatannol enhances cisplatin sensitivity in ovarian cancer via modulation of p53, X-linked inhibitor of apoptosis protein (XIAP), and mitochondrial fission. J Biol Chem. 2013;288(33):23740–50.
10. Peng L, Yang R, Wang Z, Jian H, Tan X, Li J, et al. Polyphyllin II (PPII) enhances the sensitivity of Multidrug-resistant A549/DDP cells to cisplatin by modulating mitochondrial energy metabolism. Vivo. 2024;38(1):213–25.
11. Kordias D, Kostara CE, Papadaki S, Verigos J, Bairaktari E, Magklara A. Omics analysis of chemoresistant triple negative breast Cancer cells reveals novel metabolic vulnerabilities. Cells. 2022;11:17.
12. Case KC, Schmidtke MW, Greenberg ML. The Paradoxical role of inositol in cancer: a consequence of the metabolic state of a tumor. Cancer Metastasis Rev. 2022;41(2):249–54.
13. Hsu CC, Zhang X, Wang G, Zhang W, Cai Z, Pan BS, et al. Inositol serves as a natural inhibitor of mitochondrial fission by directly targeting AMPK. Mol Cell. 2021;81(18):3803–19. e7.
14. Rahbar H, Partridge SC. Multiparametric MR imaging of breast Cancer. Magn Reson Imaging Clin N Am. 2016;24(1):223–38.
15. Kang HS, Kim JY, Kim JJ, Kim S, Lee NK, Lee JW, et al. Diffusion kurtosis MR imaging of invasive breast cancer: correlations with prognostic factors and molecular subtypes. J Magn Reson Imaging. 2022;56(1):110–20.
16. Zhang H, Li W, Fu C, Grimm R, Chen Z, Zhang W, et al. Comparison of intravoxel incoherent motion imaging, diffusion kurtosis imaging, and conventional DWI in predicting the chemotherapeutic response of colorectal liver metastases. Eur J Radiol. 2020;130:109149.
17. Sharma U, Agarwal K, Sah RG, Parshad R, Seenu V, Mathur S, et al. Can Multi-Parametric MR based approach improve the predictive value of pathological

and clinical therapeutic response in breast Cancer patients?? Front Oncol. 2018;8:319.
18. Musall BC, Adrada BE, Candelaria RP, Mohamed RMM, Abdelhafez AH, Son JB et al. Quantitative apparent diffusion coefficients from peritumoral regions as early predictors of response to neoadjuvant systemic therapy in Triple-Negative Breast Cancer. J Magn Reson Imaging. 2022;56(6):1901-9.
19. Hoffmann E, Schache D, Holtke C, Soltwisch J, Niland S, Krahling T, et al. Multiparametric chemical exchange saturation transfer MRI detects metabolic changes in breast cancer following immunotherapy. J Transl Med. 2023;21(1):577.
20. Dhakan C, Anemone A, Ventura V, Carella A, Corrado A, Pirotta E et al. Assessing the therapeutic efficacy of proton transport inhibitors in a Triple-Negative breast Cancer murine model with magnetic resonance imaging-Chemical exchange saturation transfer tumor pH imaging. Metabolites. 2023;13(11).
21. Sharma U, Danishad KK, Seenu V, Jagannathan NR. Longitudinal study of the assessment by MRI and diffusion-weighted imaging of tumor response in patients with locally advanced breast cancer undergoing neoadjuvant chemotherapy. NMR Biomed. 2009;22(1):104–13.
22. Yankeelov TE, Lepage M, Chakravarthy A, Broome EE, Niermann KJ, Kelley MC, et al. Integration of quantitative DCE-MRI and ADC mapping to monitor treatment response in human breast cancer: initial results. Magn Reson Imaging. 2007;25(1):1–13.
23. Manton DJ, Chaturvedi A, Hubbard A, Lind MJ, Lowry M, Maraveyas A, et al. Neoadjuvant chemotherapy in breast cancer: early response prediction with quantitative MR imaging and spectroscopy. Br J Cancer. 2006;94(3):427–35.
24. Rosenkrantz AB, Padhani AR, Chenevert TL, Koh DM, De Keyzer F, Taouli B, et al. Body diffusion kurtosis imaging: basic principles, applications, and considerations for clinical practice. J Magn Reson Imaging. 2015;42(5):1190–202.
25. Goldenberg JM, Pagel MD. Assessments of tumor metabolism with CEST MRI. NMR Biomed. 2019;32(10):e3943.
26. Jia Y, Wang C, Zheng J, Lin G, Ni D, Shen Z, et al. Novel nanomedicine with a chemical-exchange saturation transfer effect for breast cancer treatment in vivo. J Nanobiotechnol. 2019;17(1):123.
27. Krikken E, Khlebnikov V, Zaiss M, Jibodh RA, van Diest PJ, Luijten PR, et al. Amide chemical exchange saturation transfer at 7 T: a possible biomarker for detecting early response to neoadjuvant chemotherapy in breast cancer patients. Breast Cancer Res. 2018;20(1):51.
28. Naito S, von Eschenbach AC, Giavazzi R, Fidler IJ. Growth and metastasis of tumor cells isolated from a human renal cell carcinoma implanted into different organs of nude mice. Cancer Res. 1986;46(8):4109–15.
29. Huang Y, Lin Y, Hu W, Ma C, Lin W, Wang Z, et al. Diffusion kurtosis at 3.0T as an in vivo imaging marker for breast Cancer characterization: correlation with prognostic factors. J Magn Reson Imaging. 2019;49(3):845–56.
30. Zaric O, Farr A, Poblador Rodriguez E, Mlynarik V, Bogner W, Gruber S, et al. 7T CEST MRI: A potential imaging tool for the assessment of tumor grade and cell proliferation in breast cancer. Magn Reson Imaging. 2019;59:77–87.
31. Shen Y, Zhang X, Liu S, Xin L, Xuan W, Zhuang C, et al. CEST imaging combined with (1)H-MRS reveal the neuroprotective effects of riluzole by improving neurotransmitter imbalances in Alzheimer's disease mice. Alzheimers Res Ther. 2025;17(1):20.
32. Vucenik I, Druzijanic A, Druzijanic N. Inositol hexaphosphate (IP6) and Colon cancer: from concepts and first experiments to clinical application. Molecules. 2020;25(24).
33. Haris M, Cai K, Singh A, Hariharan H, Reddy R. In vivo mapping of brain myo-inositol. NeuroImage. 2011;54(3):2079–85.
34. Vucenik I, Shamsuddin AM. Protection against cancer by dietary IP6 and inositol. Nutr Cancer. 2006;55(2):109–25.
35. Zhao Y, Ma C, Cai R, Xin L, Li Y, Ke L, et al. NMR and MS reveal characteristic metabolome atlas and optimize esophageal squamous cell carcinoma early detection. Nat Commun. 2024;15(1):2463.
36. Belli P, Costantini M, Malaspina C, Magistrelli A, LaTorre G, Bonomo L. MRI accuracy in residual disease evaluation in breast cancer patients treated with neoadjuvant chemotherapy. Clin Radiol. 2006;61(11):946–53.
37. Rieber A, Brambs HJ, Gabelmann A, Heilmann V, Kreienberg R, Kuhn T. Breast MRI for monitoring response of primary breast cancer to neo-adjuvant chemotherapy. Eur Radiol. 2002;12(7):1711–9.
38. Zhang D, Geng X, Suo S, Zhuang Z, Gu Y, Hua J. The predictive value of DKI in breast cancer: does tumour subtype affect pathological response evaluations? Magn Reson Imaging. 2022;85:28–34.
39. Tang WJ, Yao W, Jin Z, Kong QC, Hu WK, Liang YS, et al. Evaluation of the effects of Anti-PD-1 therapy on Triple-Negative breast Cancer in mice by diffusion kurtosis imaging and dynamic Contrast-Enhanced imaging. J Magn Reson Imaging. 2022;56(6):1912–23.
40. Partridge SC, McDonald ES. Diffusion weighted magnetic resonance imaging of the breast: protocol optimization, interpretation, and clinical applications. Magn Reson Imaging Clin N Am. 2013;21(3):601–24.
41. Nogueira L, Brandão S, Matos E, Nunes RG, Loureiro J, Ramos I, et al. Application of the diffusion kurtosis model for the study of breast lesions. Eur Radiol. 2014;24(6):1197–203.
42. Deng X, Liu J, Liu L, Sun X, Huang J, Dong J. Drp1-mediated mitochondrial fission contributes to baicalein-induced apoptosis and autophagy in lung cancer via activation of AMPK signaling pathway. Int J Biol Sci. 2020;16(8):1403–16.
43. Genovese I, Carinci M, Modesti L, Aguiari G, Pinton P, Giorgi C. Mitochondria: insights into crucial features to overcome Cancer chemoresistance. Int J Mol Sci. 2021;22(9).
44. Trotta AP, Chipuk JE. Mitochondrial dynamics as regulators of cancer biology. Cell Mol Life Sci. 2017;74(11):1999–2017.
45. Weiner-Gorzel K, Murphy M. Mitochondrial dynamics, a new therapeutic target for triple negative breast Cancer. Biochim Biophys Acta Rev Cancer. 2021;1875(2):188518.
46. Baltzer P, Mann RM, Iima M, Sigmund EE, Clauser P, Gilbert FJ, et al. Diffusion-weighted imaging of the breast-a consensus and mission statement from the EUSOBI international breast Diffusion-Weighted imaging working group. Eur Radiol. 2020;30(3):1436–50.
47. Mangalhara KC, Varanasi SK, Johnson MA, Burns MJ, Rojas GR, Esparza Molto PB, et al. Manipulating mitochondrial electron flow enhances tumor immunogenicity. Science. 2023;381(6664):1316–23.
48. Mills EL, Kelly B, O'Neill LAJ. Mitochondria are the powerhouses of immunity. Nat Immunol. 2017;18(5):488–98.

Publisher's note